

# A Bionic Data-Driven Approach for Long-Distance Underwater Navigation With Anomaly Resistance

Songnan Yang<sup>ID</sup>, Xiaohui Zhang<sup>ID</sup>, Shiliang Zhang<sup>ID</sup>, Member, IEEE, Xuehui Ma<sup>ID</sup>, Wenqi Bai<sup>ID</sup>, Yushuai Li<sup>ID</sup>, Senior Member, IEEE, and Tingwen Huang<sup>ID</sup>, Fellow, IEEE

**Abstract**—Various animals exhibit accurate navigation using environmental cues. The Earth’s magnetic field has been proven to be a reliable information source for long-distance fauna migration. Inspired by the animal navigation, this work proposes a bionic and data-driven approach for long-distance underwater navigation. The proposed approach uses measured geomagnetic data for navigation and requires no GPS systems or geographical maps. Particularly, we construct and train a temporal attention-based long short-term memory (TA-LSTM) network to predict the heading angle during navigation. To mitigate the impact of geomagnetic anomalies, we develop a mechanism to detect and quantify the anomalies based on maximum likelihood estimation (MLE). We integrate the developed mechanism with the TA-LSTM and calibrate the predicted heading angles to gain resistance against geomagnetic anomalies. Using the retrieved data from the WMM model, we conduct numerical simulations with diversified navigation conditions to test our approach. The simulation results demonstrate the resilience of our navigation approach against geomagnetic anomalies, along with the precision and stability of underwater navigation in single and multiple destination missions.

**Index Terms**—Data driven, dead reckoning, geomagnetic navigation, long short-term memory (LSTM), underwater navigation.

## I. INTRODUCTION

UNDERWATER navigation empowers exploration and operation in the sea and has drawn attention in a wide range of applications such as resource survey, rescue, mapping, and underwater maintenance [1]. The navigation information is

Received 23 July 2024; revised 19 January 2025; accepted 27 January 2025. Date of publication 24 February 2025; date of current version 10 March 2025. This work was supported in part by the National Major Scientific Instrument Development Project of China under Grant 62127809, in part by the National Natural Science Foundation of China under Grant 62073258, and in part by the Basic Research in Natural Science and Enterprise Joint Foundation of Shaanxi Province under Grant 2021JLM-58. The Associate Editor coordinating the review process was Dr. Alessio De Angelis. (*Corresponding author: Xiaohui Zhang.*)

Songnan Yang, Xiaohui Zhang, and Wenqi Bai are with the School of Automation and Information Engineering and the Institute of Advanced Navigation and Electromagnetics, Xi’an University of Technology, Xi’an, Shaanxi 710048, China (e-mail: yang.son.nan@gmail.com; xhzhang@xaut.edu.cn; bayouenqy@outlook.com).

Shiliang Zhang is with the Department of Informatics, University of Oslo, 0316 Oslo, Norway (e-mail: shilianz@ifi.uio.no).

Xuehui Ma is with the School of Automation and Information Engineering, Xi’an University of Technology, Xi’an, Shaanxi 710048, China (e-mail: xuehui.yx@gmail.com).

Yushuai Li is with the Department of Computer Science, Aalborg University, 9220 Aalborg, Denmark (e-mail: yushuaili@ieee.org).

Tingwen Huang is with the Faculty of Computer Science and Control Engineering, Shenzhen University of Advanced Technology, Shenzhen 518055, China (e-mail: huangtingwen2013@gmail.com).

Digital Object Identifier 10.1109/TIM.2025.3545179

critical for marine carriers to approach the destination, conduct underwater tasks, and return to their base safely and timely. Nevertheless, due to the underwater environment where radio signals attenuate rapidly, navigation approaches used on land or in the air, e.g., the Global Navigation Satellite System (GNSS), do not work any longer [2].

Underwater navigation has been extensively investigated with numerous solutions available, including inertial, acoustic, visual matching, terrain matching, gravity matching, and geomagnetic-based navigation. However, these navigation approaches still face significant challenges in long-range navigation missions, e.g., an inertial navigation system (INS)-based approach can achieve underwater navigation without any external information. Yet, INS induces positioning deviation due to the error drift of inertial devices. This error drift accumulates over time and distance, impeding the accuracy of long-distance navigation [3]. Doppler velocity log (DVL) systems can obtain high performance in underwater navigation; however, the DVL measurements are energy-consuming, and the navigation carrier requires a large battery or frequent recharging for long-range missions [4]. The acoustic-based approach can provide accurate real-time location during the navigation but requires a signal base station to be deployed prior to the mission that does not fit for unexplored areas [5]. Visual matching navigation provides carriers like autonomous underwater vehicles (AUVs) the heading signals for the navigation, by comparing the live image from the on-board camera with a prebuilt visual map. However, the optical images can be degraded due to visibility and lighting factors especially in long-range missions, leading to a limited application scenarios with close-range mission scenarios and small areas [6].

Geophysical matching navigation approaches, such as terrain matching [2], gravity matching [7], and geomagnetic matching [8], can improve underwater navigation under various conditions. Nevertheless, these methods rely on matching navigation trajectories that require reference maps [9], [10], [11]. The terrain contour matching (TERCOM) algorithm [12] provides continuous corrections and maintains accuracy even with significant initial position errors and altimeter noise. Gravity matching compares measured gravity fields with a reference map, improving navigation robustness in areas with gravity anomalies [13]. Magnetic contour matching (MAGCOM) [14] uses the geomagnetic information for trajectory matching, which has more features than gravity and terrain. However, MAGCOM requires the geomagnetic map and is

vulnerable to environmental factors, such as solar activity and geomagnetic storms, which leads to geomagnetic anomalies that significantly affect the navigation performance over long-range missions [11]. Overall, the effectiveness of geophysical matching techniques is highly dependent on the precision and completeness of the reference map, which might be unavailable or inaccessible during long-distance missions [15].

Compared with the limitations of engineered underwater navigation approaches in long-range missions, animal navigation has shown remarkable advantages in their migratory abilities without prestored maps. Investigations reveal that various animals can navigate through thousands of kilometers merely relying on real-time environmental cues [15], [16]. During the long-distance navigation, animals can extensively utilize geomagnetic signals from the Earth for orientation and positioning [17]. Magnetic displacement experiments have demonstrated that a wide range of species, including crustaceans, fish, and birds, derive essential navigational information from these geomagnetic cues [18], [19], [20]. The animal navigation using geomagnetic information has inspired studies on bionic geomagnetic navigation approaches.

Bionic navigation has gained momentum to mimic animal navigation and utilize geomagnetic information for long-range missions. Qi et al. [21] utilized an extended Kalman filter (EKF)-based algorithm to predict heading angles using Earth's simulated magnetic dipole and gradient. While they avoided prestored maps for navigation, they neglected geomagnetic irregularities which can compromise the effectiveness of their simulations [22]. Taylor et al. [23] demonstrated a geomagnetic approach for long-distance transequatorial navigation, although their approach's performance is significantly impacted by magnetic noise. Zhang et al. [15] introduced a geomagnetic gradient-assisted evolutionary approach to enhance navigation in anomaly prone areas; yet, the method's navigation calculation suffers from ineffective computational searches. Zhang et al. [1] proposed a geomagnetic navigation method using model predictive control (MPC) for long-range navigation. While their approach requires no prior knowledge of the geographical location, they use fixed navigation parameters in heading angle prediction that hinder the adaptability of their approach, especially in geomagnetic anomaly areas where the magnetic signals vary dramatically. Qi et al. [24] developed a 2-D approach for long-distance underwater navigation using the information of regularly distributed geomagnetic gradients; however, they did not consider the situation where the carrier falls into a local area with unknown geomagnetic anomalies. da Silva et al. [25] utilized the Hampel filter approach to detect and compensate geomagnetic anomalies in the navigation. They designed the mechanism to recognize anomalies and provided a replacement for the abnormal geomagnetic information detected. In their approach, the data replacement is sensitive to the window size of their detection and the anomaly detection threshold, parameters of which cannot be adaptively adjusted according to the geomagnetic circumstance. The geomagnetic navigation without prior map issue remains challenging in that: 1) geomagnetic anomalies can vary over time and are hard to predict, making it impractical to create a reference map for long-distance geomagnetic

navigation; 2) geomagnetic anomaly is almost inevitable in long-distance missions, leading to obstacles for the navigation based on geomagnetic information; and 3) geomagnetic anomalies render the calculation of geomagnetic gradient useless, thus deteriorating the heading angle prediction based on the gradients and resulting in unnecessary travel or even failed geomagnetic navigation.

In this work, we propose a long-distance geomagnetic navigation approach with anomaly resistance. Particularly, we construct a long short-term memory (LSTM) neural network with a temporal attention mechanism (TA-LSTM) for the prediction of heading angles for navigation. The temporal attention mechanism extracts the most relevant and useful geomagnetic information to be fed to the LSTM for the model training. In this way, the proposed approach can extract the most relevant information for the navigation in areas with diverse geomagnetic characteristics. To gain resistance against geomagnetic anomalies, we use maximum likelihood estimation (MLE) to determine the divergence between the predicted heading angles by the model and the heading angle calculated based on collected geomagnetic information during the navigation. Such a divergence is weighted in an adaptive way to adjust the predicted heading angle. We integrate the anomaly detection in the navigation model in an adaptive manner, so as to enhance the efficiency of the navigation across areas with different geomagnetic features. To best of the authors' knowledge, we are the first to develop a TA-LSTM-based solution for long-distance underwater navigation using the geomagnetic information. We summarize our contribution as follows.

- 1) We propose a data-driven approach for long-distance underwater navigation that mimics animal deadreckoning. This approach leverages measured geomagnetic data for navigation and requires no geographical or geomagnetic reference maps. The designed approach offers high efficiency for geomagnetic navigation and leads to shorter travel distances compared to INS-based, evolutionary, and 2-D gradient navigation approaches.
- 2) We propose an MLE-based approach to identify geomagnetic anomalies during geomagnetic navigation. The designed approach can correct heading angles in geomagnetic anomaly areas and enhance navigation accuracy, leading to reduced sensitivity to geomagnetic abnormalities for geomagnetic navigation.

We organize our work as follows. Section II presents the mathematical description of the geomagnetic field (GF) and formulates the geomagnetic navigation problem. Section III details the proposed navigation approach with resistance to anomalies. Section IV conducts simulations under diverse navigation conditions, analyses navigation performances, and makes comparisons. We conclude our work in Section V.

## II. FUNDAMENTAL

### A. Mathematical Description of the GF

The GF is a physical field of the Earth and can be measured by a magnetometer. The GF strength  $F$  at a certain location on Earth is mainly composed of three components,  $B_m$ ,  $B_e$ ,

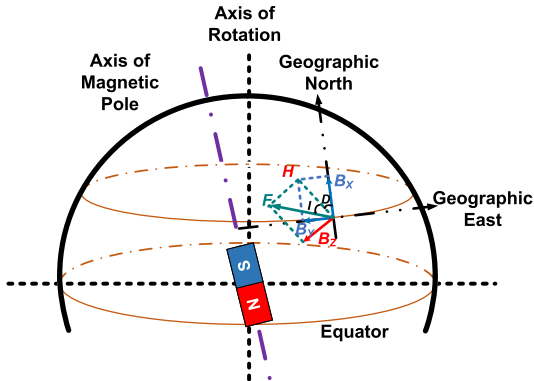


Fig. 1. Main elements in the GF.

and  $B_d$ , as shown in (1).  $B_m$  denotes the main magnetic field, which is produced by large-scale electric currents in the liquid outer core of the Earth [26].  $B_e$  means the abnormal GF generated mainly from ferrimagnetic minerals.  $B_d$  is the geomagnetic anomaly due to changes in the ionosphere and magnetosphere. While  $B_d$  for a given location is associated with solar activities and can vary dramatically over time [27],  $B_m$  and  $B_e$  are stable or hardly vary

$$F = B_m + B_e + B_d. \quad (1)$$

Fig. 1 shows the main elements in GF. A mathematical description of GF can be presented by seven geomagnetic elements, as shown in (2). Parts of those elements follow 2-D coordination, where the  $x$ -axis is along with the geographical north and the  $y$ -axis with the geographical east. Specifically, for a given location,  $F$  denotes the total strength of GF.  $H$  and  $B_Z$  are the projections of  $F$  on the horizontal plane and in the vertical direction, respectively.  $B_X$  and  $B_Y$  are the projections of  $H$  in the  $x$ - and  $y$ -axes, respectively.  $I$  is the magnetic inclination presenting the angle between  $F$  and the horizontal plane, and  $D$  is the magnetic declination presenting the angle between  $H$  and  $B_X$ . Note that geographical north is not the same as geomagnetic north. That is, the axis of the geomagnetic pole currently tilts at an angle of  $11^\circ$  with respect to the axis of Earth's rotation or geographical north

$$\left\{ \begin{array}{l} B_X = F \cos I \cos D \\ B_Y = F \cos I \sin D \\ B_Z = F \sin I \\ F = \sqrt{B_X^2 + B_Y^2 + B_Z^2} \\ H = F \cos I \\ I = \arccos(H/F) \\ D = \arccos(B_x/H). \end{array} \right. \quad (2)$$

When describing GF using the geomagnetic vector  $(B_X, B_Y, B_Z, F, H, I, D)$ , theoretically, one geomagnetic vector corresponds to a unique geographical location on the Earth [28], which lays a solid foundation for geomagnetic underwater navigation. Note that for the seven elements in the geomagnetic vector, four of them are derived. Therefore, it is possible to use less information in a geomagnetic vector to achieve navigation.

## B. Navigation and GF

Assume the actual navigation trajectory of a marine carrier, e.g., an AUV, is

$$L = \{L_o, L_1, \dots, L_{k-1}, L_k, \dots\} \quad (3)$$

where  $L_k$  denotes the location at the time instance  $k$ . Associate those locations with a 2-D coordinate, then we get  $L_k = [l_{x,k}, l_{y,k}]^T$ , where  $l_{x,k}$  and  $l_{y,k}$  are the projections of  $L_k$  in the directions of geographical north and east, respectively. Then, we have

$$\left\{ \begin{array}{l} l_{x,k+1} = l_{x,k} + \cos \theta_k \cdot V_k \\ l_{y,k+1} = l_{y,k} + \sin \theta_k \cdot V_k \end{array} \right. \quad (4)$$

where  $\theta_k$  is the heading angle of the AUV that determines the movement direction and  $V_k$  denotes the AUV velocity. Below, we present the trajectory in (3) by geomagnetic elements shown in (2). Particularly, we associate a geomagnetic vector  $S_k$  with the location  $L_k$  in (3) by combining two geomagnetic elements  $S_k = (D_k, I_k)$ , where  $D_k$  and  $I_k$  are the magnetic declination and inclination at location  $L_k$ , respectively. The relationship between adjacent declinations and inclinations is as follows:

$$\left\{ \begin{array}{l} D_{k+1} = D_k + g_{Dx,k} \cos \theta_k + g_{Dy,k} \sin \theta_k \\ I_{k+1} = I_k + g_{Ix,k} \cos \theta_k + g_{Iy,k} \sin \theta_k \end{array} \right. \quad (5)$$

where  $g_{Dx,k}$  and  $g_{Dy,k}$  are the gradients of  $D$  in the direction of geographical north and east, respectively,  $g_{Ix,k}$  and  $g_{Iy,k}$  are the gradients of  $I$  in the direction of geographical north and east [1], [15], respectively, as presented in the following equation:

$$\left\{ \begin{array}{l} g_{Dx,k+1} = \frac{D_k - D_{k-1}}{l_{x,k} - l_{x,k-1}} \\ g_{Dy,k+1} = \frac{D_{k+1} - D_k}{l_{y,k+1} - l_{y,k}} \\ g_{Ix,k+1} = \frac{I_k - I_{k-1}}{l_{x,k} - l_{y,k-1}} \\ g_{Iy,k+1} = \frac{I_{k+1} - I_k}{l_{y,k+1} - l_{y,k}}. \end{array} \right. \quad (6)$$

Based on (4)–(6), the heading angle  $\theta'_k$  at the instance  $k$  for the navigation can be derived as follows:

$$\theta'_k = \arctan \left( \frac{(I_k - I_d)g_{Dx,k} - (D_k - D_d)g_{Ix,k}}{(D_k - D_d)g_{Iy,k} - (I_k - I_d)g_{Dy,k}} \right). \quad (7)$$

The navigation can be achieved through the derivation of the heading angle iteratively toward the destination.

The navigation process can be seen as a convergence of the geomagnetic state vector  $M_k = (B_X, B_Y, B_Z, D, I)_k$  at the location  $L_k$  toward those at the destination, represented as  $M_d = (B_X, B_Y, B_Z, D, I)_d$ . In this work, we quantify this convergence using the objective function as follows:

$$F_i(M_k) = \frac{(M_{k,i} - M_{d,i})^2}{(M_{o,i} - M_{d,i})^2} \quad (8)$$

$$F(M_k) = \frac{1}{L} \sum_{i=1}^L F_i(M_k) \quad (9)$$

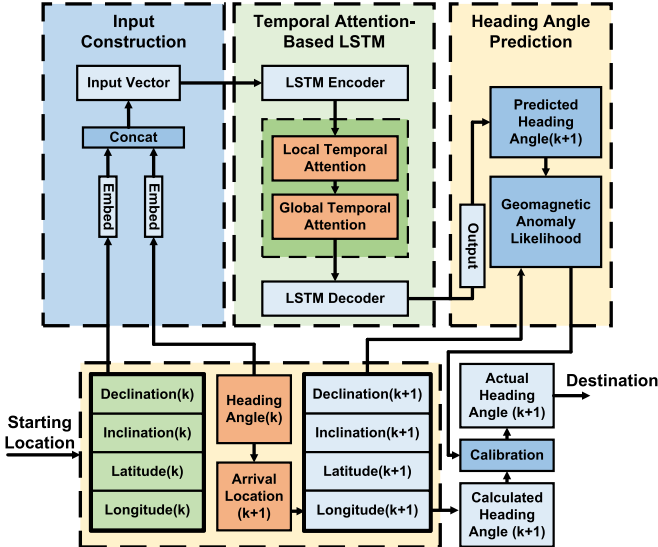


Fig. 2. Schematic of our geomagnetic navigation with TA-LSTM network and anomaly resistance.

where  $L$  is the length of  $M_k$ .  $M_{k,i}$  and  $M_{d,i}$  denote the  $i$ th element of  $M_k$  and  $M_d$ , respectively.  $M_{o,i}$  means the  $i$ th element of the geomagnetic vector at the starting point of the navigation. Note that the objective function is normalized to exclude the difference in magnitude between different geomagnetic elements. Under this objective function, the value of  $F(M_k)$  will be 0 when an AUV arrives at the destination.

Searching a unique solution in (9) is time-consuming. To avoid lengthy searching, the navigation process is terminated when the error converges within a threshold  $\varepsilon$ , as shown in (10). Increasing this threshold will decrease the navigation accuracy while increasing the success rate of arrival at the destination

$$F(M_k) \leq \varepsilon. \quad (10)$$

In the above, we describe navigation using geomagnetic information. The performance of this navigation is measured by an objective function, which determines when to terminate the navigation iteration. However, geomagnetic anomalies exist that render the calculation of the declination/inclination gradient in (6) useless, thus making the calculation of the heading angle in (7) meaningless. Therefore, there is a need to detect and compensate for geomagnetic anomalies for robust geomagnetic navigation. Our study proposes a data-driven solution that provides resilient navigation against anomalies, particularly for long-distance underwater navigation, as detailed in Section III.

### III. PROPOSED UNDERWATER NAVIGATION WITH ANOMALY RESISTANCE

This study proposes a data-driven approach that predicts the heading angle during navigation. We achieve this prediction through training a TA-LSTM network. The TA-LSTM takes input as a time series of measured geomagnetic information and calculated geographical information and outputs the heading angle toward the navigation destination. The TA-LSTM

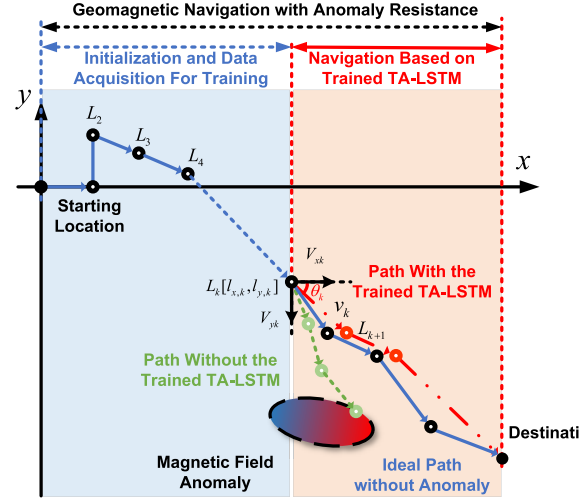


Fig. 3. Geomagnetic navigation process of the proposed TA-LSTM approach.

penalizes the weights for abnormal elements in an input time series in cases of anomalies, thus providing a robust heading angle prediction. To determine the existence of anomalies, the predicted heading angle of TA-LSTM is compared with the calculated heading angle by (7). The final heading angle to be utilized by navigation is determined on the basis of the calibration between the predicted and calculated heading angles. A high-level description of the proposed underwater navigation approach is shown in Fig. 2.

Fig. 3 demonstrates how the proposed approach with TA-LSTM works during navigation. The training of the TA-LSTM takes the input of geomagnetic declination, geomagnetic inclination, latitude, and longitude, which are all measured by a precise INS [29], [30]. The ground truth for the TA-LSTM output during the training is also provided by the INS. After the training, the TA-LSTM takes input of the declination/inclination and latitude/longitude calculated from (6) and (7), respectively, to predict the heading angle toward the destination. During navigation, we use the objective function defined in (8) and (9) along with the threshold  $\varepsilon$  to assess the proximity of the carrier to the destination. Below, we describe in detail the proposed TA-LSTM in comparison with traditional LSTM, the encoding and decoding of geomagnetic information in the TA-LSTM, and the anomaly resistance for navigation with TA-LSTM.

#### A. Description of LSTM Networks

An LSTM is a special recurrent neural network (RNN) that addresses the problem of disappearing gradients in RNNs by introducing gating mechanisms [31]. With additional memory and gate units, an LSTM is capable of extracting the inherent patterns within a series that exhibit longer intervals and delays [32]. The LSTM consists of hidden states  $h_k$  and cell memory  $c_k$ , that, respectively, store the summary of the past input sequences and control the information flow between the input and output through a gating mechanism. The calculation within an LSTM is as follows:

$$f_k = \sigma(W_f \cdot [h_{k-1}, x_k] + b_f) \quad (11)$$

$$i_k = \sigma(W_i \cdot [h_{k-1}, x_k] + b_i) \quad (12)$$

$$o_k = \sigma(W_o \cdot [h_{k-1}, x_k] + b_o) \quad (13)$$

$$g_k = \tanh(W_g \cdot [h_{k-1}, x_k] + b_g) \quad (14)$$

$$c_k = f_k \odot c_{k-1} + i_k \odot g_k \quad (15)$$

$$h_k = o_k \odot \tanh(c_k) \quad (16)$$

where  $f_k$  is the output of the forget gate that determines how much information to forget,  $i_k$  is the output of the gate that determines how much information will be used to update the network, and  $o_k$  is the output of the gate that determines how much information will be used for the network output.  $\sigma$  is a logistic sigmoid function and  $\odot$  is elementwise product, and  $x_k$  is the input vector.  $W_f$ ,  $W_i$ ,  $W_o$ , and  $W_g$  are linear transformation matrices whose parameters need to be learned, while  $b_f$ ,  $b_i$ ,  $b_o$ , and  $b_g$  are their corresponding bias vectors. We simplify the LSTM calculations as follows:

$$(h_k, c_k) = \text{LSTM}(x_k, h_{k-1}, c_{k-1}). \quad (17)$$

However, vanilla LSTM networks assign the time sequences  $x_k$  with the same weight in the input and do not distinguish the key sequences that affect the prediction most. Thus, the trained model is unable to fully utilize the geomagnetic information that has a high impact on heading angle prediction  $\theta$ .

### B. Encoding and Decoding of Geomagnetic Information With Temporal Attention in LSTM

Marine animals can selectively process external information and focus on pertinent signals during long-distance navigation [33]. We resemble such animal navigation by using TA-LSTM network. The temporal attention mechanism in the TA-LSTM can assign higher weights to the most relevant elements in the input time series. In that way, the heading angles predicted by the TA-LSTM will be based on reliable geomagnetic information that avoids the impact of geomagnetic anomalies. Below, we detail the input and output of the TA-LSTM and how it works in heading angle prediction.

This study uses a multi-input multi-output TA-LSTM, and both the input and output are time series of length  $T$ . The  $n$ th input time series is  $X_n = [x_1^n, x_2^n, \dots, x_k^n, \dots, x_T^n]$ , where

$$x_k^n = [L_k^n, S_k^n]^T \quad (18)$$

$$L_k^n = [l_{x,((n-1)*T+k)}, l_{y,((n-1)*T+k)}] \quad (19)$$

$$S_k^n = [D_{(n-1)*T+k}, I_{(n-1)*T+k}] \quad (20)$$

where  $L_k^n$  is the traveled distance at the  $((n-1)*T+k)$ th navigation iteration at the  $x$ - and  $y$ -axes, which can be obtained via (4).  $S_k^n$  denotes the magnetic declination and inclination at the  $((n-1)*T+k)$ th navigation iteration, which can be obtained via (5).

We describe the  $n$ th output of the TA-LSTM as follows:

$$Y_n = [y_1^n, y_2^n, \dots, y_k^n, \dots, y_T^n] \quad (21)$$

where

$$y_k^n = \theta_{(n-1)*T+k} \quad (22)$$

$\theta_{(n-1)*T+k}$  denotes the  $((n-1)*T+k)$ th heading angle provided by INS during the TA-LSTM training. In this

way, we obtain a collection of input time series  $X = [X_1, X_2, \dots, X_n, \dots, X_N]$  and the corresponding output time series  $Y = [Y_1, Y_2, \dots, Y_n, \dots, Y_N]$  that can feed into the training of the TA-LSTM.

The temporal attention mechanism that differentiates weights for elements in the input time series is achieved through the encoder-decoder structure in the TA-LSTM. We construct the encoder-decoder structure using two LSTM cells. The encoder structure is shown in Fig. 4. The encoder takes the  $n$ th input as  $x_k^n$  and updates the encoder state vector  $c_n^e$  and hidden vector  $h_n^e$  through (23). The local attention weight  $e_k^n$ , and the weight of importance  $a_k^n$  for the  $k$ th element in the  $n$ th input time series are calculated as follows:

$$e_k^n = V_e^T \cdot \tanh(W_e \cdot [h_{n-1}^e, c_{n-1}^e] + U_e \cdot Y_n + b_e) \quad (23)$$

$$a_k^n = f_{\text{softmax}}(e_k^n) \quad (24)$$

where  $f_{\text{softmax}}(\cdot)$  is a softmax function.  $V_e^T$ ,  $W_e$ ,  $U_e$ , and  $b_e$  are the parameters to be learned. By adjusting the attention weight  $a_k^n$ , we assign dynamic weight to the input sequence  $x_n^k$ , through which we emphasize the geomagnetic information that is more relevant to heading prediction. The hidden state and the cell state of the TA-LSTM encoder incorporating the attention weight  $h_n^e$  are calculated by

$$(h_n^e, c_n^e) = \text{LSTM}(\bar{X}_n, h_{n-1}^e, c_{n-1}^e) \quad (25)$$

where  $\bar{X}_n = (x_1^n \cdot a_1^n, x_2^n \cdot a_2^n, \dots, x_T^n \cdot a_T^n)$  is the  $n$ th input time series with local attention weight. With the encoder, the information fed into the LSTM is reconstructed, and elements in the input are differentiated with different weights. For noisy or anomalous geomagnetic data, the attention mechanism assigns a lower weight to reduce its interference with the prediction.

The TA-LSTM decoder is depicted in Fig. 5. The decoder uses the learned context from the encoder and makes predictions by attending to specific parts of the input time series. The decoder takes the hidden states from the encoder when calculating the global temporal attention weights. The global temporal attention weight  $g_n^d$  for the  $n$ th input time series is

$$l_n = V_d^T \cdot \tanh(W_d \cdot [h_{n-1}^d, c_{n-1}^d] + U_d \cdot h_n^e + b_d) \quad (26)$$

$$\beta_n = f_{\text{softmax}}(l_n) \quad (27)$$

$$g_n^d = \sum_{\tau=1}^n \beta_\tau h_\tau^e \quad (28)$$

where  $V_d^T$ ,  $W_d$ ,  $U_d$ , and  $b_d$  are the parameters to be learned in the global attention calculation and  $\beta_\tau$  is the global attention weight for the  $\tau$ th input time series.

The decoder then integrates the  $n$ th input time series with the local attention weight  $\bar{X}_n$ , the  $n$ th global attention weight  $g_n^d$ , and the  $n$ th ground truth for the output  $Y_n$ . The integrated information is fed to the input layer of the decoder LSTM, which is a fully connected (FC) layer. The calculation in this FC LSTM layer is as follows:

$$Y'_n = W_n \cdot [\bar{X}_n, g_n^d, Y_n] + b' \quad (29)$$

where  $W_n$  and  $b'$  are the weight and bias for the FC layer, respectively, and  $Y'_n$  is the calculation result of the FC layer.

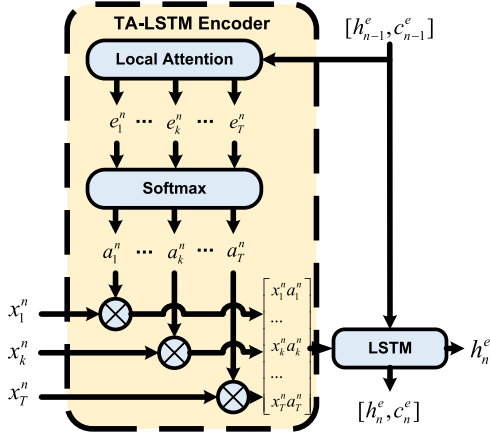


Fig. 4. Structure of encoder with local temporal attention.

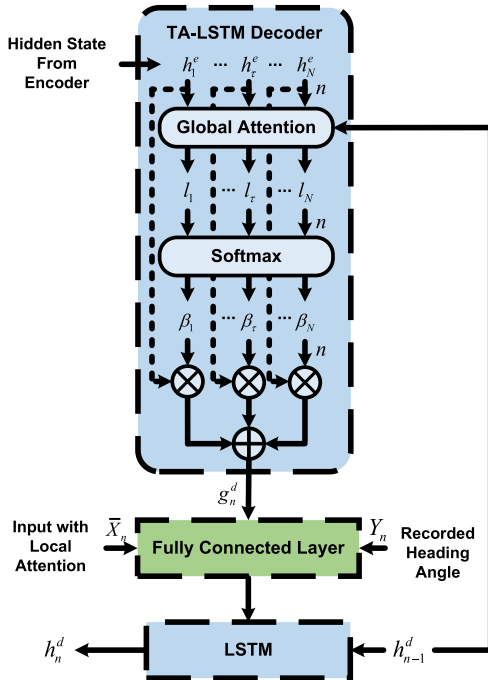


Fig. 5. Structure of decoder with global temporal attention.

The cell state and the hidden state of the decoder LSTM are calculated as follows:

$$(c_n^d, h_n^d) = \text{LSTM}(Y'_n, h_{n-1}^d, c_{n-1}^d). \quad (30)$$

Then, we use the  $n$ th cell state and the hidden state of the decoder LSTM to predict the output. The  $(n+1)$ th predicted output time series  $\bar{Y}_{n+1} = [y_1^{n+1}, y_2^{n+1}, \dots, y_k^{n+1}, \dots, y_T^{n+1}]$  is calculated as follows:

$$\bar{Y}_{n+1} = V_y^T \cdot (W_y \cdot [h_T^d, c_T^d] + b_w) + b_y \quad (31)$$

where  $W_y$  and  $b_w$  are the weight and bias for the output gate in the decoder LSTM, respectively.  $V_y^T$  and  $b_y$  are the weight and bias of an FC layer for dimension transformation. The predicted heading angle to be used in the next navigation iteration is  $\theta_k^{n+1} = \bar{Y}_k^{n+1}$ ,  $k \in \{1, 2, \dots, T\}$ .

The parameters to be learned for the TA-LSTM are identified by minimizing the loss function as follows:

$$\text{loss}(\phi) = \frac{1}{M} \sum_{m=1}^M (Y_m - \bar{Y}_m)^2 \quad (32)$$

where  $M$  is the number of time series in the training dataset and  $Y_m$  and  $\bar{Y}_m$  are the ground truth and predicted heading angles for the  $m$ th time series during the training, respectively.

### C. Geomagnetic Anomaly and Heading Angle Calibration

This section provides a further step toward resistance to navigation against geomagnetic anomalies, along with robust navigation when the amount of training data is insufficient. Particularly, we employ MLE [34] to quantify the level of geomagnetic anomaly and integrate the quantified anomaly level into heading angle prediction. We define the error vector for the  $n$ th navigation iteration as follows:

$$e^n = \frac{1}{k} \sum_{k=1}^T |\theta_k'^n - \bar{\theta}_k^n| \quad (33)$$

where  $\theta_k'^n$  and  $\bar{\theta}_k^n$  represent the  $k$ th element of the  $n$ th calculated and predicted heading angle by (7) and (31), respectively. We assume that  $\theta_k'^n \sim N(\mu, \sigma^2)$  since the geomagnetic signals are distributed in a regular way when there are no geomagnetic anomalies. We use the  $n$ th calculated heading angle sequence to estimate the parameters  $\mu$  and  $\sigma^2$  via MLE. Then, we define an anomaly weight  $\eta^n$  for the  $n$ th calculated heading angle as follows:

$$\eta^n = \exp\left(-\frac{(e^n - \mu)^T (e^n - \mu)}{\sigma^2}\right) \quad (34)$$

where  $\eta^n$  decreases when there is a dramatic deviation of geomagnetic information from expected ones and  $\eta^n$  increases when there are no geomagnetic anomalies and the geomagnetic signals distribute normally. We integrate the anomaly weight into heading angle prediction as follows:

$$\theta_k^n = \eta^n \cdot \theta_k'^n + (1 - \eta^n) \cdot \bar{\theta}_k^n. \quad (35)$$

In this way, the prediction of heading angle replies more on the calculated heading angle when the geomagnetic signals distribute normally; otherwise, it replies more on the heading angle predicted by the TA-LSTM. By using the geomagnetic anomaly weight obtained by MLE, our geomagnetic navigation approach will be able to use local information in a data driven way to correct the prediction heading angle affected by geomagnetic anomalies. Thus, the proposed navigation can still work in the case of insufficient training data samples with normally distributed geomagnetic signals. We summarize our approach in the pseudocode in Algorithm 1.

## IV. SIMULATIONS AND RESULTS

This section carries out simulations to demonstrate the performance of the proposed approach. We conduct the simulations under three navigation conditions: 1) navigation free from geomagnetic anomalies; 2) navigation with geomagnetic

**Algorithm 1** Geomagnetic Navigation With Anomaly Resistance

---

**Input:**  $S_o = [D_o, I_o]^T$ ,  $S_d = [D_d, I_d]^T$ ,  $L_o = [l_{x,o}, l_{y,o}]$ ,  
 $L_d = [l_{x,d}, l_{y,d}]$ ,  $\theta_1 = 0$ ,  $\theta_2 = 90$ ,  $\varepsilon$ ,  $V_0$ .

1 Initial input  $X_1$  and feature sequence  $Y_1$  by (2) - (7).

2 **while**  $F(S_{k+1}^n) > \varepsilon$  **do**

3     Calculate heading angle  $\theta_k^n$ ;

4     Calculate local attention weight by (23)–(24);

5     Update encoder state  $c_n^e$  and  $h_n^e$  by (25);

6     Calculate global attention weight by (26) - (28) using (32);

7     Calculate the decoder output by (29);

8     Update decoder cell and state  $c_n^d$  and  $h_n^d$  by (30);

9     Predict heading angle  $\bar{\theta}_k^n$  by (31);

10    Finalize the prediction of the heading angle  $\theta_k^n$  by (33) - (35);

11    Update  $S_{k+1}^n$  and  $L_{k+1}^n$  with  $\theta_k^n$  and  $V_k^n$  by (4).

12 **end**

**Output:**  $S_{k+1}^n$ ,  $L_{k+1}^n$ ,  $V_k$ ,  $\theta_k^n$ .

---

anomalies; and 3) navigation with multiple and consecutive destinations. We employ those diversified conditions to extensively test our approach and make comparisons. Below, we explain the specifications that apply to all three sets of simulations.

We conduct the simulations on a desktop computer (CPU: Intel Core i7-11700: 2.50 GHz; RAM: 16 Gb; and Graphics: GTX1060: 6 Gb) using MATLAB R2023a. We chose a rectangular area for the navigation simulations in the vast western Pacific, which is from 19° north latitude and 132° east longitude (19°N and 132°E) to 24° north latitude and 137° east longitude (24°N and 137°E) in the WGS84 coordinate system. According to the WMM 2020 [35], the geographical coordinates of the area can be uniquely determined by the geomagnetic information.

We use the World Magnetic Model (version 2020/1/1) [36] to retrieve geomagnetic information and generate the dataset for training. In the experimental area, we extract  $5000 \times 5000 \times 7$  geomagnetic data for the target geographic area with a grid size of 5000 and stored the data in a CSV file for the simulation. We generate geomagnetic anomaly data from the geomagnetic anomaly model GEOIST [37]. To calculate the heading angle more conveniently, we converted the obtained geomagnetic data with WGS84 coordinates into the Universal Transverse Mercator (UTM) coordinate system to facilitate underwater navigation. The conversion from WGS84 to UTM coordinate is achieved using *projwd* function in MATLAB.

The initial model is trained offline in anomaly-free areas. Then, we apply the trained model into areas with and without geomagnetic anomalies, where online training is conducted during the navigation. Note that geomagnetic navigation requires an appropriate speed of the marine carrier in the beginning, as revealed by Zhang et al. [1]. That is, if the speed is too slow, the geomagnetic gradient cannot be obtained, while a too-fast speed leads to unnecessary costs. Therefore, before

feeding the geomagnetic information in time series into the TA-LSTM model, we perform the necessary preprocessing on the geomagnetic information. First, we normalize the sequence data to a range of [0, 1] using the *mapminmax* function, avoiding the dominance of the geomagnetic information with high magnitude in the prediction. In addition, we align all the time series to the same length, ensuring that all input features are complete at each time step. We chose an initial speed  $V_0$  as 27 knots (about 50 km/h). To enable a faster convergence in the following navigation process and a nuanced speed change near the destination, we set the decay for the initial speed as

$$V_k^n = \begin{cases} \text{lr}(V_0), & \text{if } |\text{lat}_K - \text{lat}_d| \leq 0.5^\circ \& \\ & |\text{lon}_K - \text{lon}_d| \leq 0.5^\circ \\ V_0, & \text{otherwise} \end{cases} \quad (36)$$

$$K = (n - 1) * T + k \quad (37)$$

$$\text{lr}(V_0) = V_0 * d * e^{\text{int}(\frac{T-k}{sd})} \quad (38)$$

where *lr* denotes the decay function, and  $\text{lat}_K$  and  $\text{lon}_K$  represent the latitude and longitude for the  $K$ th location during the navigation, respectively. *int* means rounding down to the nearest integer, *sd* denotes the initial speed decay interval, and *d* is the decay rate.

Based on the specifications above, we conduct underwater navigation simulations with diversified navigation conditions, as detailed in Sections IV-A–IV-D.

#### A. Underwater Navigation Without Geomagnetic Anomaly

This simulation uses (22.600°N, 132.900°E) as the starting location and (20.800°N, 136.000°E) as the destination. The geomagnetic information at the starting point is  $S_o = (D_o, I_o) = [-4.321, 30.861]^T$  and at the destination as  $S_d = (D_d, I_d) = [-3.425, 27.008]^T$ . The starting location in UTM is  $L_o = [284116.65, 2500794.34]^T$  and the destination in UTM is  $L_d = [604074.88, 2300365.07]^T$ . We implement another two geomagnetic navigation approaches for comparison: the evolutionary approach by Zhang et al. [15] and the 2-D gradient approach by Qi et al. [24], with the same configurations as the work in [15] and [24], respectively. We also implement the INS-based approach, where we use the open-source PSINS toolbox [38] for the simulation. We list the configurations for the simulation in this section in Table I.

We present the simulation results in the WGS84 coordinate system in Fig. 6, demonstrating navigation trajectories of four navigation approaches. The INS-based navigation results in significant deviations in long-range missions due to accumulated errors over time, as shown in Fig. 6. Compared with the INS-based method, geomagnetic navigation approaches consistently approximate the destination. Among the geomagnetic methods, our approach achieves more stable headings and smoother trajectories than the evolutionary and 2-D geomagnetic approaches and also excels in handling geomagnetic gradients compared with the conventional BiLSTM network and results in shorter trajectories. Fig. 7 demonstrates the convergence progress of the geomagnetic information from the starting location to the destination,

TABLE I  
CONFIGURATION PARAMETERS FOR APPROACHES

Parameter	Value
Starting Location	(22.600°N, 132.900°E)
Destination	(20.800°N, 136.000°E)
Input Samples Length ( $T$ )	20
Samples of Every Iteration ( $N$ )	30
Epochs of Encoder and Decoder	100
Hidden layers of LSTM	3
Batch Size of LSTM	20
Learning Rate	0.001
Drop Factor	0.1
Training Ratio	0.8
Learn Rate Drop Period	30
Termination Condition	$\varepsilon \leq 0.02$ or 300 Iterations
Activation Function	tanh
Initial Speed	27 knots
INS Navigation Duration	$2.7191 \times 10^4$ seconds
INS Starting Attitude	pitch=0, roll=0, yaw=0
INS Speed	vE=11.8521, vN=-7.2408, vU=0 m/s

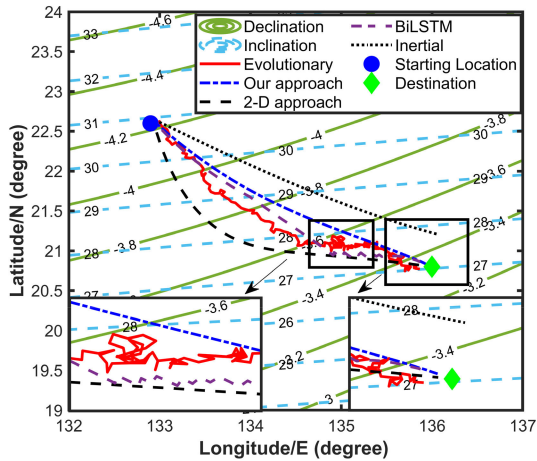


Fig. 6. Simulation results without geomagnetic anomalies.

as measured in (8). Fig. 7(a) shows that under our approach and all geomagnetic components except  $B_X$  consistently converge to the destination. In contrast, the evolutionary, 2-D, and BiLSTM approaches, require longer iterations and show less uniform convergence. Specifically, the  $B_X$  component across all approaches fails to converge as expected, while our approach demonstrates lower fluctuation and reduced values for  $B_X$  compared with the remaining. The evolutionary approach suffers from nonuniform geomagnetic information convergence [Fig. 7(b)], leading to unpredictable heading fluctuations. The 2-D approach [Fig. 7(c)] is with low efficiency in the convergence since its calculations rely on geomagnetic gradients and yet neglect location geomagnetic information. The BiLSTM approach [Fig. 7(d)] works well in the beginning of the navigation, but tends to overfit and induces unstable headings near the destination.

To quantitatively assess the performance of the considered navigation approaches, we define the following metrics to indicate the navigation efficiency, accuracy, and stability of the navigation, and the results of which are summarized in Table II.

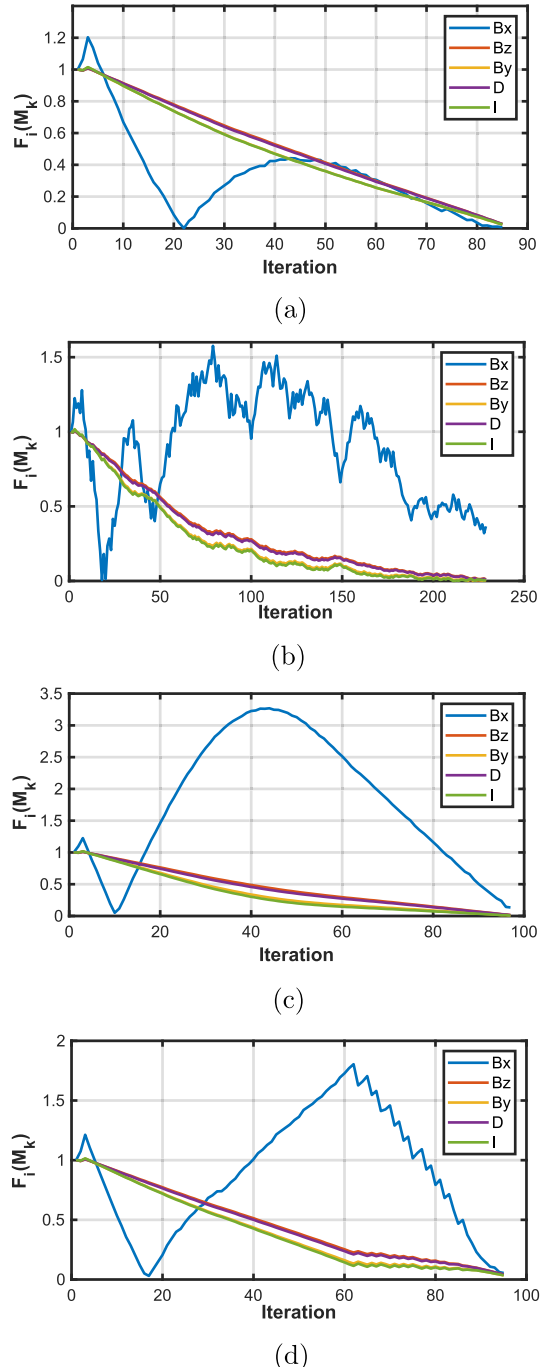


Fig. 7. Convergence of the navigation demonstrated by  $F_i(M_k)$ , where  $i \in \{1, 2, \dots, 5\}$ ,  $k$  denotes the iteration number. (a) Our approach convergence curve. (b) Evolutionary approach convergence curve. (c) 2-D approach convergence curve. (d) BiLSTM approach convergence curve.

- 1) *Terminal Location:* This metric assesses the accuracy of the arrival at the destination when the navigation termination conditions are met.
- 2) *Traveled Distance:* Sum of the distances covered during the navigation. This metric indicates the rationality of the navigated path.
- 3) *Navigation Iteration:* This parameter indicates the iterations required for the carrier to reach the destination and serves as a gauge for the efficiency of the navigation.

- 4) *Heading Angle Variance*: Denoted by  $\theta_{\text{var}}$  and calculated according to (39), this metric evaluates the fluctuation in the heading angle throughout the navigation

$$\theta_{\text{var}} = \sum_{n=1}^N \sum_{k=1}^T \left( \theta_k^n - \bar{\theta}_k^n \right) / K_t \quad (39)$$

where  $T$  and  $N$  denote the length of a single output time series by the prediction and the total number of output time series, respectively.  $K_t$  is the total number of locations traversed in the navigation.  $\theta_k^n$  and  $\bar{\theta}_k^n$  mean the ground truth and the predicted heading angle for the  $k$ th location of the  $n$ th output time series, respectively.

- 5) *Navigation Deviation*: Calculated by (40), this metric measures the deviation between the actual and optimal trajectories, providing insights into the precision of the navigation system

$$\text{Deviation} = \frac{\|L_d - L_{K_t}\|}{\|L_d - L_o\|} \times 100\% \quad (40)$$

where  $K_t$  is the total number of locations traversed in the navigation.  $L_o$ ,  $L_d$ , and  $L_{K_t}$  are the origin, destination, and arrival locations for navigation in the UTM coordinates, respectively.  $\|\cdot\|$  denotes the euclidean distance.

From the quantitative results in Table II, the proposed approach significantly outperforms the remaining in multiple performance indicators. Particularly, our approach reduces navigation iterations by 62.8%, 12.3%, and 10.5% compared with the evolutionary, 2-D gradient, and BiLSTM approaches, respectively. Furthermore, our approach achieves a remarkable reduction in the travel distance of 46.2% compared with the evolutionary approach (707.996 km), 11.1% to the 2-D approach (428.495 km), and 9.56% to the BiLSTM approach (421.011 km). This reduced travel distance confirms the ability of our approach to generate a more direct trajectory that decreases energy expenditure. Also, our approach enhances the stability in heading angle variance by 98.27%, 55.65%, and 62.56% compared with the evolutionary (6.1709), 2-D gradient (0.2399), and BiLSTM (0.2842) approaches, respectively. Through these quantitative evaluations, our approach shows fast convergence, reduced distance traveled in the navigation, and smooth headings during the navigation. This indicates a substantial improvement in geomagnetic navigation compared with the evolutionary, 2-D gradient, and BiLSTM methods.

Although the heading variance of the geomagnetic approaches (including our approach) is larger than that of the INS-based navigation, the latter has an insufficient navigation performance, demonstrated by its much larger deviation from the destination at the arrival. As a comparison, our approach improves navigation accuracy by reduction in navigation deviation of 68.2% compared with the evolutionary approach (4.13%), 50.5% to the 2-D (2.65%), and 59.4% to the BiLSTM approach (3.23%). These improvements highlight the advancements in our approach over both inertial and the remaining geomagnetic navigation approaches.

### B. Navigation With Geomagnetic Anomalies

Geomagnetic anomalies are complex, changeable, and unpredictable, and they are almost inevitable in long-distance

TABLE II  
COMPARISON OF UNDERWATER NAVIGATION  
WITHOUT GEOMAGNETIC ANOMALIES

Approach	Terminal Location	traveled Distance (km)	Navigation Iteration	Heading Variance	Navigation Deviation
Our approach	(20.812°N, 135.954°E)	380.721	85	0.1064	1.31%
Evolutionary	(20.889°N, 135.884°E)	707.996	229	6.1709	4.13%
2-D approach	(20.862°N, 135.930°E)	428.495	97	0.2399	2.65%
BiLSTM	(20.851°N, 135.896°E)	421.011	95	0.2842	3.23%
Inertial	(21.142°N, 136.124°E)	377.652	-	0.0100	10.59%

navigation. To evaluate whether the navigation approaches work in the geomagnetic anomaly region, we generate geomagnetic anomalies using the GEOIST toolbox anomaly function [37] shown in (41), and we use VERDE [39] to integrate the generated anomalies in the geomagnetic information in the target area. We delineate the area of geomagnetic anomalies within 20°–23°N and 133°–136°E, which is on the anticipated navigation route. The anomaly is distributed as follows:

$$B_e = 3 \cdot (1-x)^2 \cdot e^{(-x^2-(y+1)^2)} - 10 \cdot \left( \frac{x}{5} - x^3 - y^5 \right) \cdot e^{(-x^2-y^2)} - \frac{1}{3} \cdot e^{(-(x+1)^2-y^2)} \quad (41)$$

where  $x$ ,  $y$ , and  $z$  follow the directions of  $B_X$ ,  $B_Y$ , and  $B_Z$ , respectively. By increasing the geomagnetic strength in  $B_X$ ,  $B_Y$ , and  $B_Z$  600, 400, and 200 times, as shown in Fig. 8, respectively. With the generated anomalies, we implement the geomagnetic navigation of evolutionary and 2-D navigation approaches as well as the proposed approach to check how these methods work in the presence of geomagnetic anomalies. We also implement the TA-LSTM with the Hampel approach [25]—a commonly used method for filtering geomagnetic anomalies—to examine the effectiveness of our anomaly detection mechanism. Furthermore, we also replace the TA-LSTM by a BiLSTM structure to analyze how the temporal attention mechanism contributes to the navigation. In the simulation with geomagnetic anomalies, the navigation will stop when the termination condition is satisfied, regardless of whether the AUV has reached its destination. We set the detection window and anomaly threshold of the Hampel approach as 20 and 1, respectively.

Fig. 9 shows the navigation trajectories under the considered approaches and the impact of geomagnetic anomalies on the navigation. We observe that INS-based navigation remains unaffected by these anomalies, while the geomagnetic approaches show navigation deviations to different levels. Specifically, the evolutionary approach is vulnerable and tends to fall into a local optimal solution in geomagnetic anomaly areas, resulting in failed navigation. The 2-D gradient approach depends on reliable geomagnetic information of  $D$  and  $I$  for the navigation. As a result, the 2-D approach cannot maintain a steady heading in the geomagnetic anomaly area and fails to navigate. The BiLSTM-based approach cannot well adapt

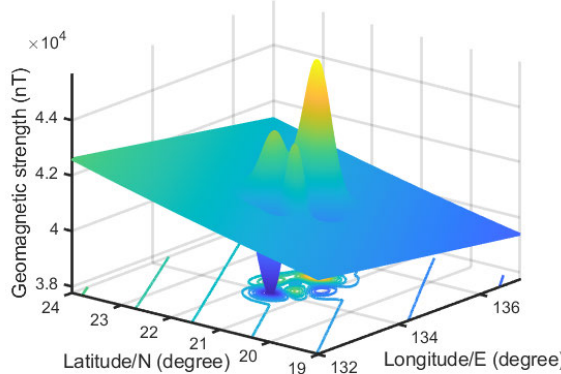


Fig. 8. Visualization of the geomagnetic anomaly for the simulation.

TABLE III

PERFORMANCE COMPARISON OF UNDERWATER NAVIGATION UNDER GEOMAGNETIC ANOMALIES

Approach	Terminal Location	Traveled Distance (km)	Navigation Iteration	Heading Variance	Navigation Deviation
Our approach	(20.926°N, 135.974°E)	397.194	89	0.1225	3.76%
Hampel	(20.957°N, 135.789°E)	433.172	109	0.1842	4.23%
Evolutionary	(21.249°N, 135.871°E)	1197.951	299	318.8745	13.63%
2-D approach	(21.507°N, 134.194°E)	1199.081	299	236.6445	53.82%
BiLSTM	(21.633°N, 134.158°E)	1197.338	299	67.4476	56.22%

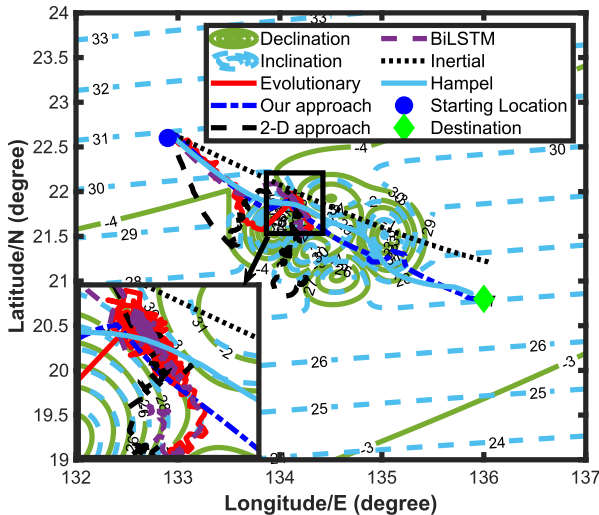


Fig. 9. Simulation results under geomagnetic anomaly.

to the geomagnetic features in the anomaly area, resulting in navigation failure in the local anomaly region. In contrast, the proposed approach and Hampel approach are able to navigate through the geomagnetic anomalies and arrive the destination, though they both experience fluctuations when crossing the geomagnetic anomalies. We also observe that compared with Hampel, our approach is more effective and navigates the carrier with a flatter and shorter trajectory from the origination to the destination.

To quantify the performance of different approaches for navigation in geomagnetic anomaly regions, we use the same metrics as in Section IV-A to gain quantitative navigation results. Fig. 10 shows the convergence of geomagnetic information under the five considered approaches. In comparison, our approach in Fig. 10(a) shows the stable convergence of the geomagnetic information even in fields with strong geomagnetic anomalies. The anomalies in *D* and *I* are effectively controlled and sound convergence is observed under the Hampel approach, as shown in Fig. 10(b). The evolutionary approach [see Fig. 10(c)] converges faster than the 2-D [see Fig. 10(d)], yet both of them converge to a local optimum and fail to navigate through the geomagnetic anomaly area. While the BiLSTM-based approach in Fig. 10(e) can predict the heading accurately when outside geomagnetic anomalies, it shows fluctuations when encountering anomalies.

The results in Table III provide a quantitative comparison between the considered approaches under geomagnetic anomalies. It is evident that the proposed approach and the Hampel approach perform better than the evolutionary, 2-D and BiLSTM approaches. Particularly, our approach achieves the most accurate terminal location (20.926°N, 135.974°E), followed by the Hampel approach (20.957°N, 135.789°E). Both the arrival location of Hampel and the proposed approach are considerably closer to the destination than the evolutionary (21.249°N, 135.871°E), 2-D (21.507°N, 134.194°E), and BiLSTM (21.633°N, 134.158°E) approaches. The total traveled distance of our approach is the shortest at 397.194 km, compared with 433.172, 1197.951, 1199.081, and 1197.338 km for the Hampel, evolutionary, 2-D, and BiLSTM approaches, respectively. Our approach demonstrates a navigation deviation of only 3.76%, which is better than the Hampel (4.23%), inertial (10.59%), evolutionary (13.63%), 2-D (53.82%), and BiLSTM (56.22%) approaches. The lower navigation deviation shows that our approach has the ability to navigate the AUV through significant geomagnetic anomalies.

### C. Simulation Results With Measurement Errors in the Navigation

This simulation incorporates measurement errors in the navigation for a more realistic navigation performance analysis. Particularly, we inject Gaussian white noise with zero mean value into the geomagnetic measurements and test and discuss the reliability and stability of the proposed method using the Monte Carlo method [24]. According to the available information on measurement errors in commercial magnetometers [40], [41], [42], common sensor measurement errors range from 10 pT to 100 nT. Therefore, we randomly construct the measurement error in the range of 10–100 nT to simulate the effect of measurement error on the TA-LSTM model. We collect the results from 50 Monte Carlo simulations and record all the navigation trajectories, as shown in Fig. 11.

We observe from Fig. 11 that under the measurement noise conditions, there are fluctuations in the heading especially when the carrier is close to the destination. Even though, in the Monte Carlo simulation test, the navigation trajectories

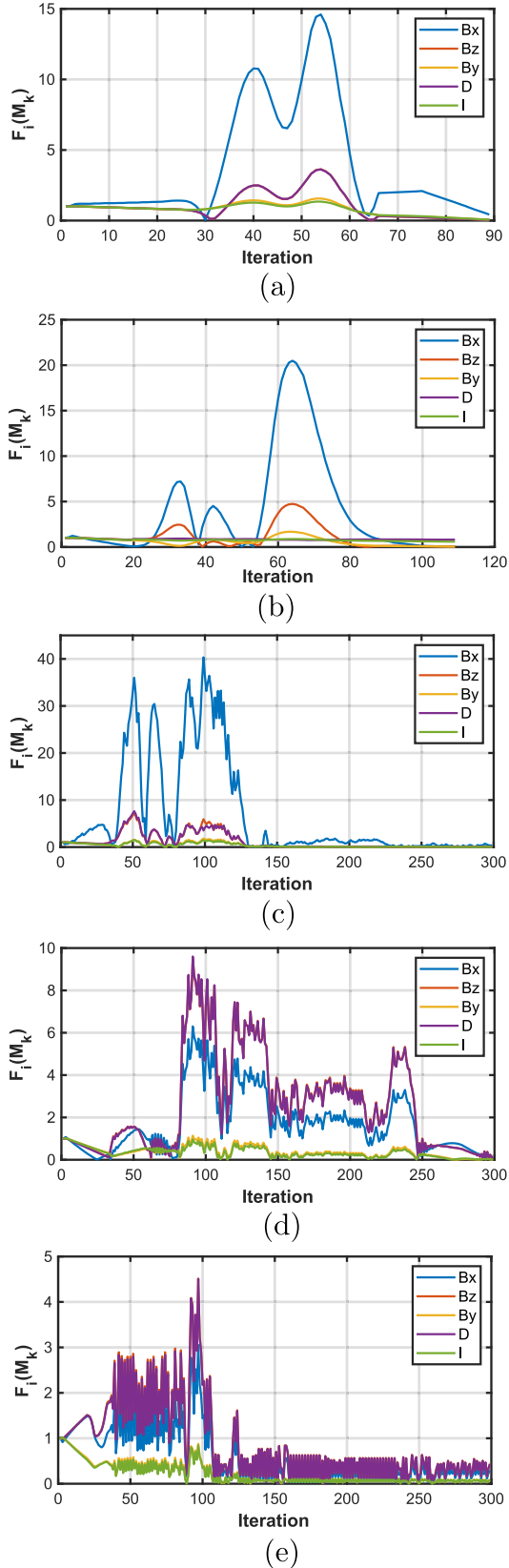


Fig. 10. Convergence of the navigation demonstrated by  $F_i(M_k)$ , where  $i \in \{1, 2, \dots, 5\}$ ,  $k$  denotes the iteration number. (a) Our approach convergence curve. (b) Hampel approach convergence curve. (c) Evolutionary approach convergence curve. (d) 2-D approach convergence curve. (e) BiLSTM approach convergence curve.

are stable, and our method can guide the navigator to the target stably. To further demonstrate the proposed approach,

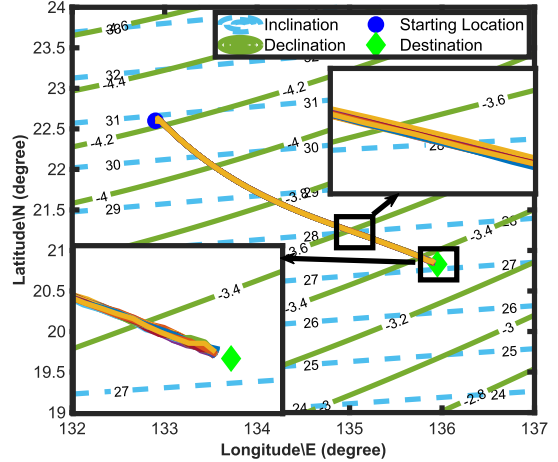


Fig. 11. Trajectories of 50 times Monte Carlo simulations.

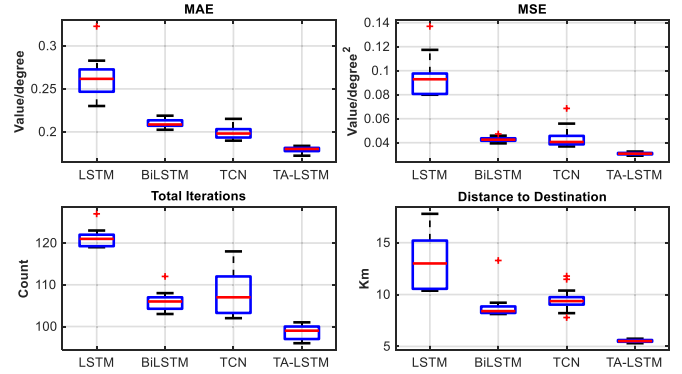


Fig. 12. Statistical box plot for the result of 50 Monte Carlo simulations with measurement errors in the navigation.

we compare our TA-LSTM model with the following three methods: 1) temporal convolutional network (TCN) [43] model; 2) traditional LSTM model without attention mechanism; and 3) BiLSTM model. The statistical results are presented in Fig. 12.

In the test result in Fig. 12, the proposed approach demonstrates lower median values within a narrow range for all the indicators of MAE and MSE for the navigation deviation, total navigation iterations, and the distance of the carrier to the destination at the arrival. The results indicate more accurate and stable heading angle predictions by the TA-LSTM model compared with LSTM, BiLSTM, and TCN, i.e., our approach requires the fewest navigation iterations, indicating a faster convergence than LSTM, BiLSTM, and TCN. Our method also brings more direct routes indicated by the navigation deviation, and improved accuracy of the arrival at the destination. This result shows that our method outperforms traditional LSTM, BiLSTM, and TCN models when considering measurement errors in the navigation.

#### D. Navigation With Multiple Destination

This simulation considers the practical scenario with multiple destinations for a single navigation mission. This simulation is free from geomagnetic anomalies, and during this simulation, the carrier has to navigate under different

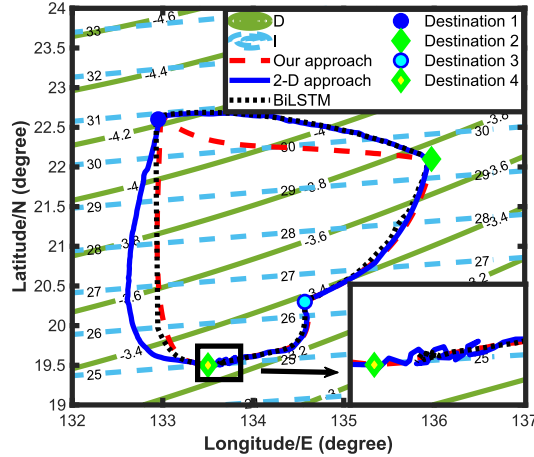


Fig. 13. Simulation results for multideestination navigation.

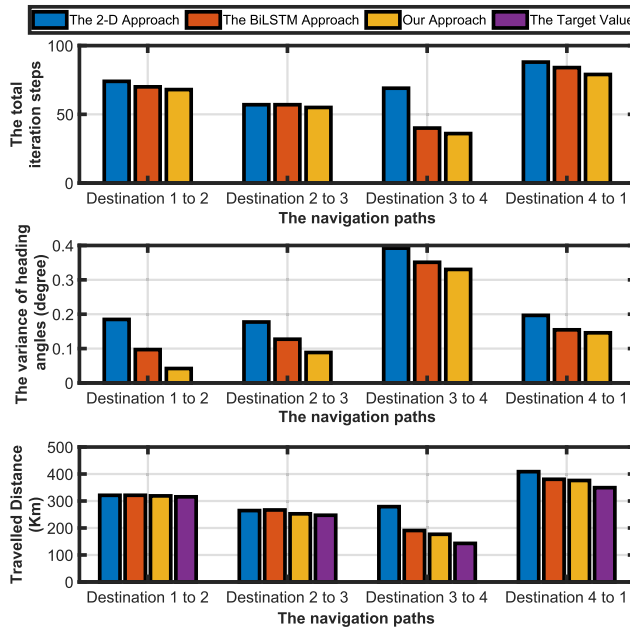


Fig. 14. Statistics for the simulation results in multideestination underwater navigation.

geomagnetic conditions, i.e., to navigate with different angles to the direction of the geomagnetic signals in the same mission. We only compare our approach with the 2-D approach and the BiLSTM approach in this simulation, since the evolutionary approach requires setting different constraint parameters for different destinations. In this simulation, the navigation commences from Destination 1 ( $22.600^{\circ}\text{N}$ ,  $132.900^{\circ}\text{E}$ ) to Destination 2 ( $22.100^{\circ}\text{N}$ ,  $136.00^{\circ}\text{E}$ ), to Destination 3 ( $20.3^{\circ}\text{N}$ ,  $134.600^{\circ}\text{E}$ ), then to Destination 4 ( $19.500^{\circ}\text{N}$ ,  $133.500^{\circ}\text{E}$ ), and finally returns to Destination 1. We use the same simulation settings as in Sections IV-A and IV-B. We relax the termination condition for the arrival at each destination as  $\varepsilon = 0.05$  for continuous navigation across submissions.

We visualize one simulation result in Fig. 13, where we show the trajectories under the considered navigation approaches. The result implies that all three navigation

approaches can accomplish the multideestination mission yet with different traveled distances. To quantitatively evaluate the navigation performance, we statistically analyze the total navigation iterations, the variance of heading angle, and the total traveled distance during the navigation. We present the average results of 50 runs of the method in Fig. 14. Through the statistics, we observe that our approach provides a 17.36% reduction in the average navigation iteration, a 36.19% reduction in heading angle variance, and an 11.72% decrease in traveled distance compared to the 2-D gradient method. Our approach also provides a 5.18% reduction in the average navigation iteration, a 16.87% reduction in heading angle variance, and a 3.02% decrease in traveled distance compared with the BiLSTM-based approach. Note that our approach merely leads to 6.15% extra traveled distance in the entire mission compared with the target value. In summary, our proposed approach requires fewer navigation iterations, covers less distance, and maintains more stable heading angles for multideestination navigation compared with the 2-D and BiLSTM-based approaches.

## V. CONCLUSION

We propose a TA-LSTM-based geomagnetic approach for long-distance underwater navigation. We leverage measured geomagnetic data and avoid any pre-stored maps for navigation. We develop a mechanism to detect and quantify geomagnetic anomalies and calibrate the heading angle prediction by the TA-LSTM. The proposed approach can learn and adapt the geomagnetic features in single and multideestination navigation and is resistant against geomagnetic anomalies during long-range missions. We plan to expand and further check our approach in other scenarios where GPS is weak or not available, e.g., during underground mining operations. We also consider the extensions where a high accuracy of arrival is required for geomagnetic navigation where precise operations are associated with the navigation.

Beyond the advantages, we reflect that the initialization of our approach depends on geomagnetic information without anomalies, while this condition might not hold in real navigation. Such limitation is augmented when the learned model is applied to a new area with significant different geomagnetic characteristics from the source area where the model is trained. To address the challenge, future studies might need to analyze the generalizability of a trained navigation model when transferring the learned knowledge across areas and navigation conditions. For future work, we also suggest integrated underwater navigation, e.g., the combination of geomagnetic navigation with INS, sonar, or imagery approach where established tools are available, so as to achieve robust navigation. The combined approach necessitates the analysis of the impact of the switch between navigation approaches on the overall navigation performance and the effectiveness of transferring navigation information across domains of navigation tools and techniques.

## REFERENCES

- [1] Y. Zhang, X. Liu, M. Luo, and C. Yang, "Bio-inspired approach for long-range underwater navigation using model predictive control," *IEEE Trans. Cybern.*, vol. 51, no. 8, pp. 4286–4297, Aug. 2021.

- [2] J. Melo and A. Matos, "Survey on advances on terrain based navigation for autonomous underwater vehicles," *Ocean Eng.*, vol. 139, pp. 250–264, Jul. 2017.
- [3] A. J. Canciani, "Magnetic navigation on an F-16 aircraft using online calibration," *IEEE Trans. Aerosp. Electron. Syst.*, vol. 58, no. 1, pp. 420–434, Feb. 2022.
- [4] A. B. Phillips et al., "Autosub long range 1500: A continuous 2000 km field trial," *Ocean Eng.*, vol. 280, Jul. 2023, Art. no. 114626.
- [5] J. W. Choi, A. V. Borkar, A. C. Singer, and G. Chowdhary, "Broadband acoustic communication aided underwater inertial navigation system," *IEEE Robot. Autom. Lett.*, vol. 7, no. 2, pp. 5198–5205, Apr. 2022.
- [6] B. Zhang, D. Ji, S. Liu, X. Zhu, and W. Xu, "Autonomous underwater vehicle navigation: A review," *Ocean Eng.*, vol. 273, Apr. 2023, Art. no. 113861.
- [7] Z. Wang, Y. Huang, M. Wang, J. Wu, and Y. Zhang, "A computationally efficient outlier-robust cubature Kalman filter for underwater gravity matching navigation," *IEEE Trans. Instrum. Meas.*, vol. 71, pp. 1–18, 2022.
- [8] P. Ding and X. Cheng, "A new contour-based combined matching algorithm for underwater terrain-aided strapdown inertial navigation system," *Measurement*, vol. 202, Oct. 2022, Art. no. 111870.
- [9] Z. Chen et al., "A new geomagnetic matching navigation method based on multidimensional vector elements of Earth's magnetic field," *IEEE Geosci. Remote Sens. Lett.*, vol. 15, no. 8, pp. 1289–1293, Aug. 2018.
- [10] N. Xu, L. Wang, T. Wu, and Z. Yao, "An innovative PSO-ICCP matching algorithm for geomagnetic navigation," *Measurement*, vol. 193, Apr. 2022, Art. no. 110958.
- [11] Z. Chen et al., "Geomagnetic vector pattern recognition navigation method based on probabilistic neural network," *IEEE Trans. Geosci. Remote Sens.*, vol. 61, 2023, Art. no. 5909608.
- [12] J. P. Golden, "Terrain contour matching (TERCOM): A cruise missile guidance aid," in *Image Processing for Missile Guidance*, vol. 0238, T. F. Wiener, Ed., Bellingham, WA, USA: SPIE, Dec. 1980, pp. 10–18.
- [13] B. Wang, B. L. Yu, Z. Deng, L. Wu, and M. Fu, "A particle filter-based matching algorithm with gravity sample vector for underwater gravity aided navigation," *IEEE/ASME Trans. Mechatronics*, vol. 21, no. 3, pp. 1399–1408, Jun. 2016.
- [14] A. Pakhomov, A. Anashina, D. Heyers, D. Kobylkov, H. Mouritsen, and N. Chernetsov, "Magnetic map navigation in a migratory songbird requires trigeminal input," *Sci. Rep.*, vol. 8, no. 1, pp. 1–6, Aug. 2018.
- [15] J. Zhang, T. Zhang, H.-S. Shin, J. Wang, and C. Zhang, "Geomagnetic gradient-assisted evolutionary algorithm for long-range underwater navigation," *IEEE Trans. Instrum. Meas.*, vol. 70, pp. 1–12, 2021.
- [16] M. Geva-Sagiv, L. Las, Y. Yovel, and N. Ulanovsky, "Spatial cognition in bats and rats: From sensory acquisition to multiscale maps and navigation," *Nature Rev. Neurosci.*, vol. 16, no. 2, pp. 94–108, Jan. 2015.
- [17] N. F. Putman, "Animal navigation: Seabirds home to a moving magnetic target," *Current Biol.*, vol. 30, no. 14, pp. R802–R804, Jul. 2020.
- [18] J. L. Gould, "Animal navigation: A map for all seasons," *Current Biol.*, vol. 24, no. 4, pp. R153–R155, Feb. 2014.
- [19] W. T. Schneider, F. Packmor, O. Lindecke, and R. A. Holland, "Sense of doubt: Inaccurate and alternate locations of virtual magnetic displacements may give a distorted view of animal magnetoreception ability," *Commun. Biol.*, vol. 6, no. 1, p. 187, Feb. 2023.
- [20] L. C. Naisbett-Jones, N. F. Putman, J. F. Stephenson, S. Ladak, and K. A. Young, "A magnetic map leads juvenile European eels to the Gulf stream," *Current Biol.*, vol. 27, no. 8, pp. 1236–1240, Apr. 2017.
- [21] X. Qi et al., "Bioinspired in-grid navigation and positioning based on an artificially established magnetic gradient," *IEEE Trans. Veh. Technol.*, vol. 67, no. 11, pp. 10583–10589, Nov. 2018.
- [22] Z. Zhao, T. Hu, W. Cui, J. Huangfu, C. Li, and L. Ran, "Long-distance geomagnetic navigation: Imitations of animal migration based on a new assumption," *IEEE Trans. Geosci. Remote Sens.*, vol. 52, no. 10, pp. 6715–6723, Oct. 2014.
- [23] B. K. Taylor, K. J. Lohmann, L. T. Havens, C. M. F. Lohmann, and J. Granger, "Long-distance transequatorial navigation using sequential measurements of magnetic inclination angle," *J. Roy. Soc. Interface*, vol. 18, no. 174, Jan. 2021, Art. no. 20200887.
- [24] X. Qi, K. Xu, Z. Xu, H. Li, and L. Ran, "Geographic true navigation based on real-time measurements of geomagnetic fields," *IEEE Trans. Geosci. Remote Sens.*, vol. 61, 2023, Art. no. 5917810.
- [25] M. V. da Silva, K. J. Pinheiro, A. Ohlert, and J. Matzka, "Analysis of geomagnetic observatory data and detection of geomagnetic jerks with the MOSFiT software package," *Geosci. Instrum., Methods Data Syst.*, vol. 12, no. 2, pp. 271–283, Dec. 2023.
- [26] T. Schwaiger, N. Gillet, D. Jault, M. Istan, and M. Mandea, "Wave-like motions and torques in Earth's core as inferred from geomagnetic data: A synthetic study," *Phys. Earth Planet. Interiors*, vol. 346, Jan. 2024, Art. no. 107104.
- [27] Y. Wang et al., "Effects of strong geomagnetic storms on the ionosphere and degradation of precise point positioning accuracy during the 25th solar cycle rising phase: A case study," *Remote Sens.*, vol. 15, no. 23, p. 5512, Nov. 2023.
- [28] A. V. Komolkin, P. Kupriyanov, A. Chudin, J. Bojarinova, K. Kavokin, and N. Chernetsov, "Theoretically possible spatial accuracy of geomagnetic maps used by migrating animals," *J. Roy. Soc. Interface*, vol. 14, no. 128, Mar. 2017, Art. no. 20161002.
- [29] B. Liu, S. Wei, J. Lu, J. Wang, and G. Su, "Fast self-alignment technology for hybrid inertial navigation systems based on a new two-position analytic method," *IEEE Trans. Ind. Electron.*, vol. 67, no. 4, pp. 3226–3235, Apr. 2020.
- [30] J. Xu, H. He, F. Qin, and L. Chang, "A novel autonomous initial alignment method for strapdown inertial navigation system," *IEEE Trans. Instrum. Meas.*, vol. 66, no. 9, pp. 2274–2282, Sep. 2017.
- [31] S. Hochreiter and J. Schmidhuber, "Long short-term memory," *Neural Comput.*, vol. 9, no. 8, pp. 1735–1780, 1997.
- [32] K. Zhu, Y. Li, W. Mao, F. Li, and J. Yan, "LSTM enhanced by dual-attention-based encoder-decoder for daily peak load forecasting," *Electr. Power Syst. Res.*, vol. 208, Jul. 2022, Art. no. 107860.
- [33] Y.-F. Liu, Y.-L. Li, T.-F. Xing, D.-X. Xue, and J.-X. Liu, "Genetic architecture of long-distance migration and population genomics of the endangered Japanese eel," *iScience*, vol. 27, no. 8, Aug. 2024, Art. no. 110563.
- [34] I. J. Myung, "Tutorial on maximum likelihood estimation," *J. Math. Psychol.*, vol. 47, no. 1, pp. 90–100, Feb. 2003.
- [35] A. Chulliat, W. Brown, and P. Alken, "The U.S./U.K. world magnetic model for 2020–2025: Technical report," Nat. Centers Environ. Inf., Asheville, NC, USA, Tech. Rep. 24390, 2020.
- [36] NCEI Geomagnetic Modeling Team and British Geological Survey, *World Magnetic Model 2020*, NOAA National Centers for Environmental Information, Asheville, NC, USA, 2020.
- [37] CEA Gravity Team of Institute of Geophysics, *Geoist*, Institute of Geophysics China Earthquake Administration, Beijing, China, 2018.
- [38] S. Yun, Z. Yao, and M. Lu, "On-the-fly ambiguity resolution method for pseudolite/INS integration based on double-difference square observations," *GPS Solutions*, vol. 25, no. 4, pp. 1–14, Aug. 2021.
- [39] L. Uieda, "Verde: Processing and gridding spatial data using Green's functions," *J. Open Source Softw.*, vol. 3, no. 30, p. 957, Oct. 2018.
- [40] J. S. Bennett et al., "Precision magnetometers for aerospace applications: A review," *Sensors*, vol. 21, no. 16, p. 5568, Aug. 2021.
- [41] R. Xie et al., "Noise estimation in vector magnetic data derived from airborne vector magnetic system," *Geophysics*, vol. 85, no. 4, pp. J71–J83, Jun. 2020.
- [42] J. Ge et al., "Real-time mitigation of measurement noise arising from geomagnetic background interferences for a coil vector magnetometer," *IEEE Trans. Instrum. Meas.*, vol. 72, pp. 1–10, 2023.
- [43] S. Gopali, F. Abri, S. Siami-Namini, and A. S. Namin, "A comparison of TCN and LSTM models in detecting anomalies in time series data," in *Proc. IEEE Int. Conf. Big Data (Big Data)*, Dec. 2021, pp. 2415–2420.



**Songnan Yang** received the M.S. degree in control science and engineering from Xi'an University of Technology, Xi'an, China, in 2020, where he is currently pursuing the Ph.D. degree.

His current research interests include geomagnetic navigation, machine learning, and signal processing.



**Xiaohui Zhang** received the B.S. degree in industrial automation, the M.S. degree in control science and engineering, and the Ph.D. degree from Xi'an University of Technology, Xi'an, China, in 1995, 2002, and 2009, respectively.

He is currently a Professor with the Department of Information and Control, Xi'an University of Technology. His recent research interests include advanced navigation, unmanned systems, signal processing, and pattern recognition.



**Wenqi Bai** received the M.S. degree in control science and engineering from Xi'an University of Technology, Xi'an, China, in 2021, where he is currently pursuing the Ph.D. degree.

His current research interests include digital twins, reinforcement learning, and geomagnetic navigation.



**Shiliang Zhang** (Member, IEEE) received the Ph.D. degree in electrical engineering from Xi'an Jiaotong University, Xi'an, China, in 2018.

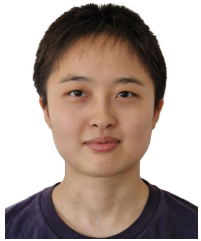
He previously worked as a Post-Doctoral Researcher at the Chalmers University of Technology, Gothenburg, Sweden, in the field of privacy-preserving machine learning approaches in-vehicle networks. He is currently a Post-Doctoral Researcher with the Department of Informatics, University of Oslo, Oslo, Norway. His current research focuses on energy informatics, machine/deep learning, system control, and anomaly detection.



**Yushuai Li** (Senior Member, IEEE) received the B.S. degree in electrical engineering and automation, and the Ph.D. degree in control theory and control engineering from Northeastern University, Shenyang, China, in 2014 and 2019, respectively.

He is currently an Assistant Professor with the Department of Computer Science, Aalborg University, Aalborg, Denmark. His main research interests include distributed optimization and control, machine learning, digital twin, and their applications in integrated energy and transportation systems.

Dr. Li received the Best Paper Awards from *Journal of Modern Power Systems and Clean Energy* and the 2023 International Conference on Cyber-Energy Systems and Intelligent Energies (ICCSIE).



**Xuehui Ma** received the B.S. degree in electrical engineering and automation, the M.S. degree in control engineering, and the Ph.D. degree in control theory and control engineering from the School of Automation and Information Engineering, Xi'an University of Technology, Xi'an, China, in 2014, 2017, and 2022, respectively.

Her current research focuses on stochastic control, dual control, robust control, and anomaly detection.



**Tingwen Huang** (Fellow, IEEE) received the B.S. degree in mathematics from Southwest Normal University, Chongqing, China, in 1990, the M.S. degree in applied mathematics from Sichuan University, Chengdu, China, in 1993, and the Ph.D. degree in mathematics from Texas A&M University at College Station, College Station, TX, USA, in 2002.

He was a Professor with Texas A&M University at Qatar, Doha, Qatar, from July 2009 to August 2024. He is currently a Professor with Shenzhen University of Advanced Technology, China. His research interests include neural networks, complex networks, chaos and dynamics of systems, and their applications.